

Supporting Information

Engineering nanoporous Ag/Pd core/shell interfaces with ultrathin Pt doping for efficient hydrogen evolution reaction over a wide pH range

C. Yang^{∇a,c}, H. Lei^{∇a}, W.Z. Zhou^b, J. R. Zeng^a, Q. B. Zhang^{a,b*}, Y.X. Hua^{a,b} and C. Y. Xu^{a,b}

^a Key Laboratory of Ionic Liquids Metallurgy, Faculty of Metallurgical and Energy Engineering, Kunming University of Science and Technology, Kunming, 650093, P.R. China

^b State Key Laboratory of Complex Nonferrous Metal Resources Cleaning Utilization in Yunnan Province, Kunming 650093, P.R. China

^c Low-dimensional Materials and Devices Laboratory, Tsinghua-Berkeley Shenzhen Institute (TBSI), Tsinghua University, Shenzhen, Guangdong 518055, P. R. China

*Corresponding author. Tel: +86-871-65162008; fax: +86-871-65161278.

E-mail address: qibo Zhang@kmust.edu.cn (Q.B. Zhang)

1. Experimental

1.1 Chemicals and materials

Choline chloride (ChCl, 98%) was dried under vacuum for at least 6 h to remove moisture before use. Ethylene glycol (EG, 99%), zinc chloride (ZnCl_2 , 99.5%), palladium chloride (PdCl_2 , Pd~60%), sodium phosphate monobasic (NaH_2PO_4 , 99.5%), sodium phosphate dibasic (Na_2HPO_4 , 99.5%), and potassium hydroxide (KOH, 99.5%) were used as received. Ag wires (0.5 mm in diameter, 99.99%), Ag foils (1 mm in thickness, 99.99%) and sulfuric acid (H_2SO_4 , 96%) were purchased from Sinopharm Chemical Reagent Co., Ltd. Commercial Pt/C (20 wt.% Pt) was bought from Sigma-Aldrich (St. Louis, MO, USA). High purity deionized water ($18.2 \text{ M}\Omega \text{ cm}^{-1}$) was used to prepare electrolyte for HER catalytic measurements. The deep eutectic solvent, Ethaline, was prepared by mixing and stirring the ChCl and EG in a molar ratios 1:2 at 353 K until a homogeneous, colorless liquid was formed.

1.2 Preparation of NPA substrate, Pd@NPA, and Pt-Pd@NPA

The nanoporous Ag (NPA) substrate was fabricated by an in-situ electrochemical alloying/dealloying process similar to our previous report, which involves galvanostatic electrodeposition of Zn on a smooth Ag substrate (wires or foils) in Ethaline containing 0.1 M ZnCl_2 at 373 K to form binary Ag-Zn alloys, and subsequently followed by in-situ selectively stripping the active Zn component from the surface alloys with an appropriate potential to create 3D hierarchical bicontinuous NPA films. After dealloying, the as-obtained NPA sample was washed with acetone and deionized water to remove organic residuals, and air dried. The synthesis of Pd@NPA was conducted via a facile galvanic replacement reaction (GRR) approach from Ethaline containing Pd precursor, where the NPA was served as both sacrificial template and reducing agent. Typically, a NPA sample with an efficient area of 0.158 cm^2 was immersed in 10 mL Ethaline containing 2 mM PdCl_2 at 353 K for a given immersion time. It is worth mentioning the microstructure of the NPA films including ligament and pore sizes can be flexibly tuned by varying synthesis parameters such as deposition temperature, current/charge density, and dealloying temperature. Moreover, the galvanic reaction time plays a crucial role in tuning the mass loading and the microtopography of the resulting Pd@NPA samples, which were systematically investigated and given in the following sections.

The Pt-Pd@NPA catalyst was prepared by a potential cycling (cyclic voltammetric scan) activation procedure. Briefly, the activation process was carried out in a conventional three-electrode cell with a N_2 -saturated 0.5 M H_2SO_4 solution at 298 K. The as-prepared Pd@NPA (geometric area = 0.158 cm^2), Pt rod (exposed surface area = 0.314 cm^2) and Ag/AgCl (3.0 M KCl) were used as the working, counter and reference electrodes, respectively. The applied potential for activation varied from -200 to 200 mV vs. Ag/AgCl at a scan rate of 100 mV s^{-1} with various cycles. After activation, the product was washed with deionized water for several times and air dried for further characterizations.

1.3 Characterization

X-ray diffraction (XRD) patterns were recorded on a Rigaku X-ray diffractometer (MiniflexII Desktop) with Cu $K\alpha$ radiation. X-ray photoelectron spectra (XPS) were collected on a PHI 550 type spectrometer using Al $K\alpha$ as the exciting source. The microstructure and elemental compositions of the prepared samples were characterized using a field emission scanning electron microscope (FE-SEM, NOVA NanoSEM 450) equipped with an energy-dispersive

X-ray (EDS) system at 15 kV. High-resolution transmission electron microscopy (HRTEM) images, EDS mapping profiles as well as high annular dark field transmission electron microscopy (HAADF-STEM) images were collected on a Tecnai G2 TF30 transmission microscope at 200 kV. The topological changes of the samples during the activation process were recorded by a tapping mode atomic force microscope (AFM, SPI3800N). The Pd and Pt contents in the samples were detected by inductively coupled plasma mass spectroscope (ICP-MS, Perkin-Elmer Elan DRC-e, USA). Gas product analysis was performed on a gas chromatograph (Agilent 7820 A, USA).

1.4 Electrochemical measurements

The electrocatalytic measurements were carried out in acidic (0.5 M H₂SO₄, pH=0), alkaline (1.0 M KOH, pH=14) and neutral (1.0 M PBS pH=7) solutions using a standard three-electrode setup at 298 K controlled by a CHI 760D electrochemical workstation. Before measurement, the electrolyte was bubbling by high-purity H₂ for at least 30 minutes to remove residual O₂. The as-prepared Pt-Pd@NPA was directly used as the working electrode. A graphite flag electrode and an Ag/AgCl (3.0 M KCl) electrode were used as the counter electrode and the reference electrode, respectively. Electrochemical impedance spectroscopy (EIS) analysis was measured at a given overpotential over a frequency range from 5 mHz to 100 kHz with an AC voltage amplitude of 5 mV. All potential vs. Ag/AgCl electrode was transformed to the reversible hydrogen electrode (RHE) according to $E_{RHE} = E_{Ag/AgCl} + 0.208 + 0.059 \times \text{pH V}$. Linear scan voltammetry (LSV) was performed at a scan rate of 5 mV s⁻¹. The iR compensation caused by voltage drop was corrected based on the solution resistance obtained from EIS measurement in the same electrochemical cell. The electrochemical double layer capacitance (Cdl) was evaluated to measure the electrochemical active surface area (ECSA) of the samples. A series of CVs were conducted in the potential range from 0.35 V to 0.45 V vs. RHE at various scan rates of 20 - 200 mV s⁻¹ to collect the capacitance charging and discharging currents. The commercial available Pt/C catalyst was prepared as follows: 5 mg Pt/C catalyst and 35 μL 5 wt% Nafion were dispersed in 1mL ethanol by 30 min sonication. Then 38 μL catalyst ink was drop cast on a Ag foil (working area: 1.0 cm²) with the Pt mass loading of 38 μg cm⁻².

1.5 Calculation of the turnover frequency (TOF)

The TOF can be calculated according to the following equation:¹⁻³

$$TOF = \frac{j * S_{geometric}}{2F * n} = \frac{\text{number of } H_2 \text{ turnovers}}{\text{number of active metal ions}} \quad (1)$$

where j is the current (A) derived from linear sweep measurement, $S_{geometric}$ is the geometric surface area of the electrode, F is the Faradic constant (96485.3 C mol⁻¹) and n is the number of active sites (mol). The factor 2 is based on the consideration that two electrons are required to form one hydrogen molecule. For both Pt-Pd@NPA and Pd@NPA samples, the experimental date and calculations reveal that Ag atom has negligible HER activity. Thus, we assume that every Pd and Pt metal atom serves as catalytic active site (n).

The number of H₂ turnovers was calculated according to the following equation:^{4,5}

$$\#H_2 = \left(j \frac{\text{mA}}{\text{cm}^2} \right) \left(\frac{1\text{C s}^{-1}}{1000 \text{ mA}} \right) \left(\frac{1\text{mol e}^-}{96485.3 \text{ C}} \right) \left(\frac{1\text{mol } H_2}{2 \text{ mol e}^-} \right) \left(\frac{6.022 \times 10^{23} H_2 \text{ molecules}}{1\text{mol } H_2} \right) = 3.12 \times 10^{15} \frac{H_2/s}{\text{cm}^2} \text{ per } \frac{\text{mA}}{\text{cm}^2} \quad (2)$$

The number of metal ions was determined from ICP-MS analysis.

For Pd@NPA-GRR-0.5 h sample with a mass loading of $35.56 \mu\text{g cm}^{-2}$

$$n_{Pd} = \frac{m_{Pd}}{M_{Pd}} = \frac{35.56 \times 10^{-6} \text{g cm}^{-2}}{106.45 \text{g mol}^{-1}} \times 6.023 \times 10^{23} = 2.011 \times 10^{17} \text{ atoms} \quad (3)$$

Thus, the number of Pd is 2.011×10^{17} metal atoms.

For the sample, Pt-Pd@NPA-GRR-0.5 h after 4000th cycles activation with a mass loading of $32.53 \mu\text{g cm}^{-2}$ Pd (1.841×10^{17} metal atoms) and $4.96 \mu\text{g cm}^{-2}$ (1.53×10^{16} metal atoms)

$$n_{Pd} = \frac{m_{Pd}}{M_{Pd}} = \frac{32.53 \times 10^{-6} \text{g cm}^{-2}}{106.45 \text{g mol}^{-1}} \times 6.023 \times 10^{23} = 1.841 \times 10^{17} \text{ atoms} \quad (4)$$

$$n_{Pt} = \frac{m_{Pt}}{M_{Pt}} = \frac{4.96 \times 10^{-6} \text{g cm}^{-2}}{195.08 \text{g mol}^{-1}} \times 6.023 \times 10^{23} = 1.53 \times 10^{16} \text{ atoms} \quad (5)$$

Thus, the number of Pd and Pt are 1.841×10^{17} and 1.53×10^{16} , respectively.

1.6 Calculation details

All structures and electronic energies were calculated based on plane-wave density functional theory (DFT) performed using the CASTEP module with ultrasoft-pseudopotentials in Material Studio 8.0 of Accelry Inc. The generalized gradient approximation (GGA) with the Perdew-Wang 1991(PW91) exchange-correlation functional and a 450 eV cut-off kinetic energy was assigned to the plane-wave basis set. Periodic boundary conditions with dipole correction were used in all cases, with at least 20 Å of vacuum in the z-direction to separate the slab from its periodic images. We adopted Ag (111) slab with three layers consisting of 43 atoms. Of the three layers, the top two layers of the slab were allowed to relax. For the geometric optimization, the structure was relaxed until the total force on each atom was less than 0.05 eV/Å. $3 \times 3 \times 1$ Monkhorst-pack-grid was used for the k-point sampling of the slab. The pseudomorphic Pt or Pd overlayers (Pd@NPA, Pt@NPA) were similarly constructed, i.e., Ag substrate slab with 20 Å, in which the top layer of Ag atoms was replaced by Pd atoms to form a monolayer to investigate the synergistic effect of Ag-Pd. The adsorption of H atom on slab surface was analyzed based on the most favorable adsorption configurations.

The Gibbs-energy (ΔG_H) is calculated as:⁶

$$\Delta G_H = \Delta E_H + \Delta E_{ZPE} - T\Delta S \quad (6)$$

where ΔE_H is the adsorption energy of H species from DFT calculations. ΔE_{ZPE} and ΔS are the zero point energy difference and the entropy difference between the adsorbed state and the gas phase, respectively, and T is the system temperature.

2. Synthesis of NPA by in-situ electrochemical alloying/dealloying

Nanoporous metals (NPMs) with a high surface area show intriguing properties that have been extensively studied for various applications in functional materials.⁷⁻¹⁰ Numerous strategies including the utilization of templates, electrochemical dealloying and electrodeposition¹¹ have been proposed to synthesize NPMs, among which dealloying, involving the selective etching of one or more active components from their alloy precursors in corrosive acidic or alkaline solutions, is demonstrated to be capable of producing bulk three-dimensional (3D) bicontinuous NPMs. In our previous investigations,^{12, 13} nanoporous copper (NPC) films are fabricated by in-situ electrochemical alloying/dealloying of Cu-Zn surface alloys from ChCl-Urea-based (Reline) and ChCl-EG-based (Ethaline) deep eutectic solvents (DESS) with zinc salts (ZnO or ZnCl_2) as alloy inductive precursors. The dealloying

processing in DESs can efficiently circumvent the issues suffering in the conventional ILs and promise a green and simple route for the preparation of NPMs. Herein, we propose to fabricate 3D bicontinuous NPA films from Ethaline by the above-mentioned alloying/dealloying approach, which are expected to function as versatile supports for electrocatalytic applications.

2.1 Cyclic voltammogram investigation

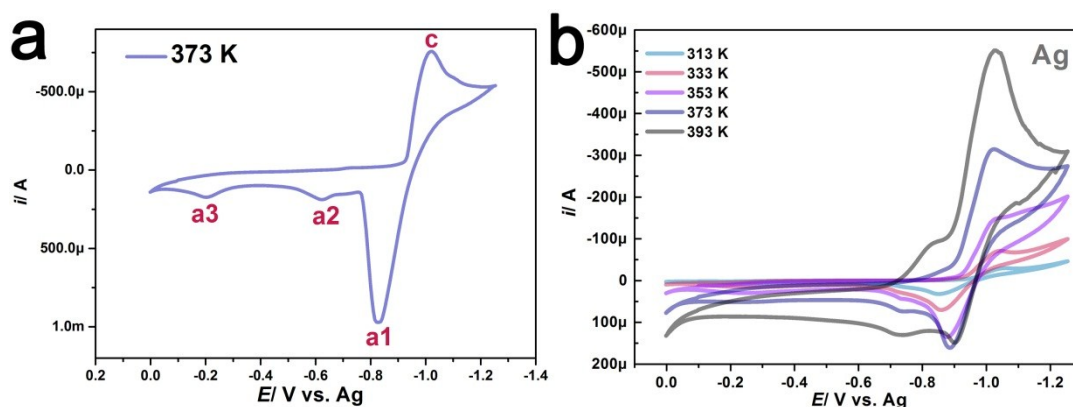


Figure S1. CVs recorded on an Ag electrode in Ethaline containing 0.1 M ZnCl₂ at (a) 373 K and (b) various temperatures (313 to 393 K)

Cyclic voltammograms (CVs) were firstly performed to disclose the electrochemical behavior of Zn²⁺/Zn⁰ couple and the formation of Ag-Zn binary alloys on the Ag surface from Ethaline containing 0.1 M ZnCl₂. As shown in Figure S1a, the typical CV for the electrochemical deposition and stripping behaviors of Zn at 373 K was investigated, the cathodic peak, c, and the corresponding anodic peak a1 are attributed to the deposition and stripping of Zn element. The other two stripping waves, a2 and a3, are associated with the anodic dissolution of the zinc that has alloyed with the Ag substrate, indicating the formation of Ag-Zn surface alloys. As expected, a higher operation temperature can facilitate the formation of Ag-Zn surface alloys,^{12, 13} where the enhanced anodic stripping current of the Ag-Zn alloys suggests more effective formation of surface alloys due to the inter-diffusion of Zn and Ag more sufficiently (Figure S1b). It can be concluded that the selection potential of Zn for creating NPA films should be positive than that of anodic stripping potential of Ag-Zn surface (a3) and negative than that of anodic stripping potential of Ag substrate (around 0 V vs. Ag).

2.2 Electrochemical alloying process investigation

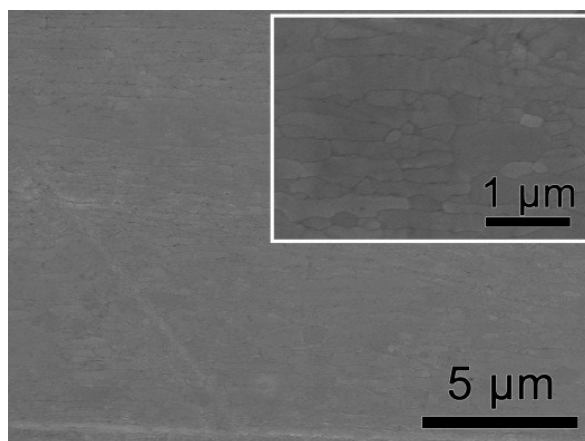


Figure S2. SEM image of the smooth Ag film. Inset shows the corresponding large magnification SEM image.

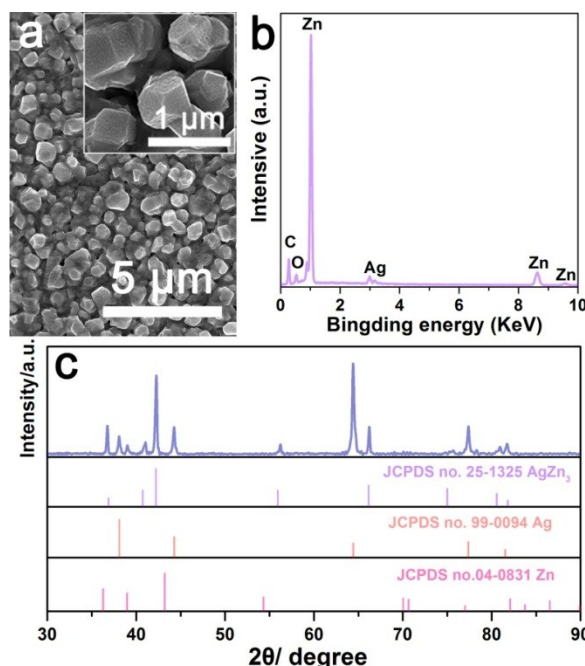


Figure S3. (a) SEM image of Zn-deposited Ag sample (inset shows the large magnification SEM image), (b) the corresponding EDS of Zn-deposited sample, (c) XRD patterns of the Zn-deposited Ag sample. The Zn-deposited Ag sample was obtained by electrodeposition at 1.0 mA cm^{-2} with 2.5 C cm^{-2} at 373 K from Ethaline containing 0.1 M ZnCl_2 .

Figure S2 shows the SEM image of a smooth Ag substrate, revealing the flat structure of Ag substrate. After Zn deposition, the Ag surface is fully covered by Zn crystal with clear grain boundaries, as shown in Figure S3a. The associated EDS spectrum also indicates that Zn is successfully deposited on the Ag substrate with Zn as the dominant element on the surface (Figure S3b). Moreover, the XRD pattern of as-deposited Zn sample (Figure S3c) exhibits the diffraction peaks of Ag substrate and pure Zn, and characteristic peaks for AgZn_3 alloy (JCPDS No. 25-1325), confirming the electrochemical formation of surface alloy during galvanostatic deposition process of Zn on the Ag surface.

For further investigations, the effects of the deposition current density, charge density and dealloying temperature on the microstructure were characterized. Depending on the deposition conditions, NPA films with various porous structures were obtained (Figures S4 and S5). With regard to the applied current density during deposition, a lower current density generally implies a relatively slow deposition rate, which provides more time

for the deposited Zn to percolate deeper into the bulk Ag substrate to form a thicker Ag-Zn surface alloy films. As a result, a thicker porous structure is obtained after dealloying. In the present case, well-defined 3D, open and bicontinuous NP structures (Figure S4) can be obtained at various applied current density (from 0.25 to 1.0 mA cm⁻²) by electrodepositing of Zn with 2.5 C cm⁻² at 373 K and followed by dealloying process under the same condition (at 0.0 V vs. Ag at 373 K for 3000 s). To obtain a relatively fast deposition rate, deposition current density of 1.0 mA cm⁻² is preferred.

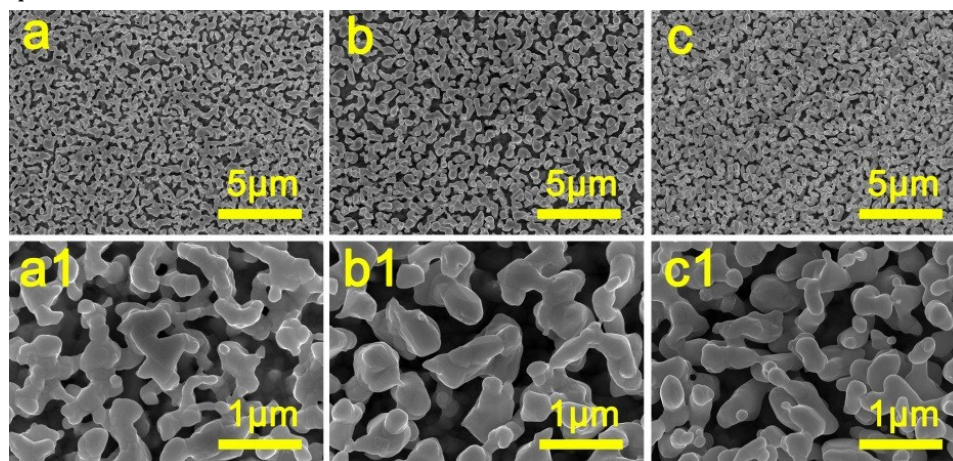


Figure S4. SEM images of the NPA films obtained by electrodepositing Zn with 2.5 C cm⁻² at various constant current densities at 373 K followed by in situ electrochemical dealloying operation at 0.0 V vs. Ag at 373 K for 3000 s. (a) 0.25 mA cm⁻², (b) 0.5 mA cm⁻² and (c) 1.0 mA cm⁻².

In the case of the applied charge during Zn deposition, the amount of Zn electrodeposited is found to play an important role in controlling the final porous structures of the NPA after subsequent dealloying process (Figure S5). When the charge density (amount) of the deposited Zn is 0.625 C cm⁻², the Ag-Zn alloy film obtained on the Ag surface is thin and resulting films display sparsely distributed ligaments (Figure S5a,a1). When the deposited Zn is 1.25 C cm⁻², an interconnected porous structure with an increase in porosity is obtained (Figure S5b,b1). Moreover, when the applied charge density is increased to 2.5 C cm⁻², the resulting post-dealloyed sample exhibits the expected 3D bicontinuous NP structure (Figure S5c,c1). Further increase on the charge density to 5.0 C cm⁻² has little effect on the morphologies of the obtained NPA (Figure S5d,d1). Because of the obtained well-defined architecture, the films deposited at a current density of 1.0 mA cm⁻² with 2.5 C cm⁻² is used for the subsequent studies described in the work.

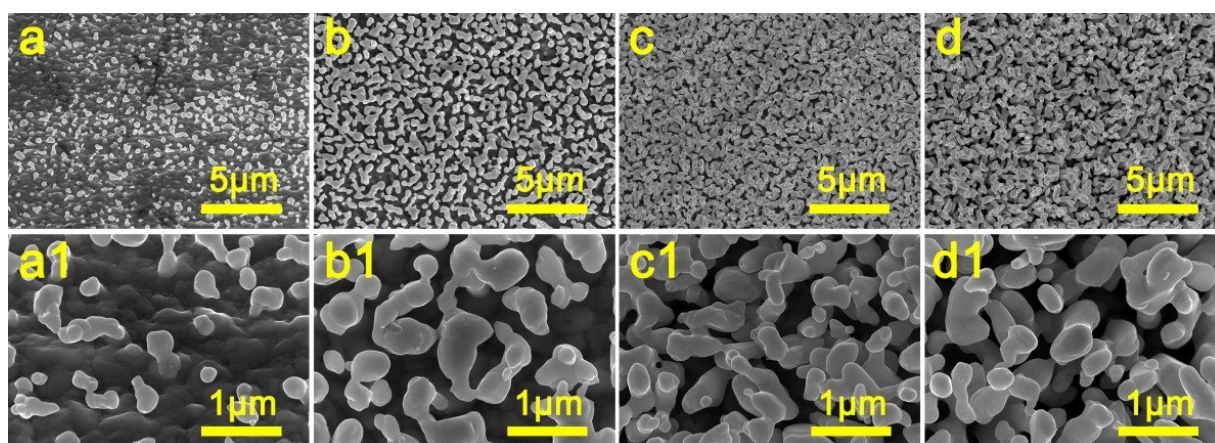


Figure S5. SEM images of the NPA films obtained by electrodepositing Zn with various charge densities at 1.0 mA cm^{-2} and 373 K, and followed by in situ electrochemical dealloying operation at 0.0 V vs. Ag at 373 K for 3000 s. (a) 0.625 C cm^{-2} , (b) 1.25 C cm^{-2} , (c) 2.5 C cm^{-2} and (d) 5.0 C cm^{-2} .

2.3 Electrochemical dealloying process investigation

The effect of dealloying temperature on the whole fabrication process was also investigated. The anodic stripping behavior during the dealloying process at various temperatures (303-373 K) is illustrated in Figure S6, with the corresponding SEM images of the dealloyed samples shown in Figure S7a-d. It is obvious that a higher temperature is benefit for the dealloying process, leading to markedly increase the initial dealloying current at short times for the selective dissolution of zinc from the Ag-Zn surface alloys (Figure S6). This result is related with a decrease in viscosity of this Ethaline DES at a higher temperature, which facilitates the surface diffusion of the Ag and Zn atoms.

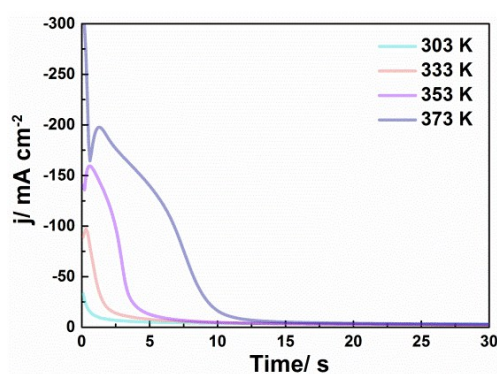


Figure S6. Anodic dealloying stripping current-time curves of Zn-deposited Ag sample that was prepared by electrodepositing 2.0 C cm^{-2} Zn at 1.0 mA cm^{-2} and 373 K, followed by electrochemical dealloying at 0.0 V vs. Ag at different temperatures (indicated).

Dealloying performed at lower temperatures of 303 and 333 K exhibit sluggish dissolution rates due to the lower mass transfer, and result in porous structures with agglomerated Ag particles and large amounts of undissolved Zn components on the ligaments (Figure S7a,b). Increasing the temperature to higher temperatures of 353 and 373 K, the surfaces become more regular (Figure S7c,d). Both the pore size and ligament size are found to increase with increasing the dealloying temperature (Figure S7e). These results indicate that this dealloying process is highly temperature dependent and exhibits a surface diffusion-controlled roughening mechanism.^{14, 15} To obtain a regular porous structure with open pores, a dealloying temperature of 373 K is employed in the subsequent experiments.

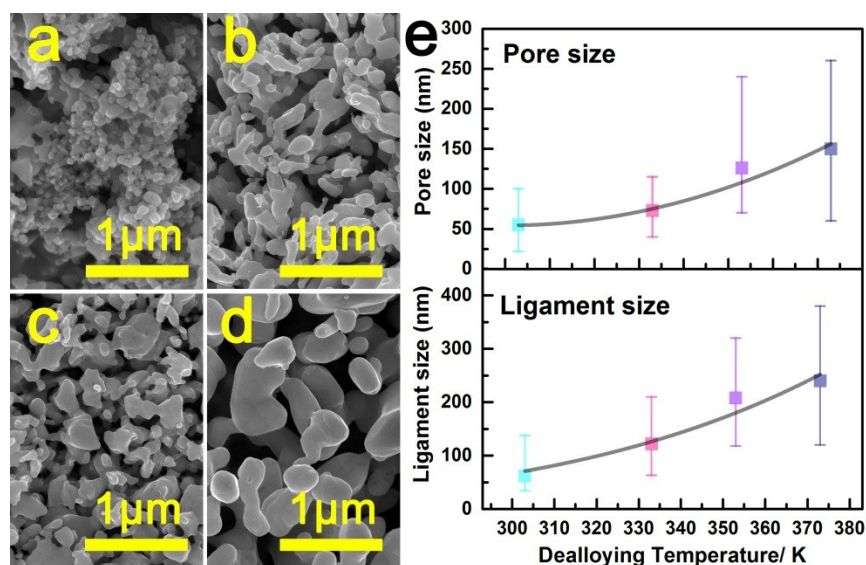


Figure S7. SEM images of the NPA films that were prepared by electrodepositing 2.5 C cm^{-2} Zn at 1.0 mA cm^{-2} and 373 K , and followed by anodic dealloying at 0.0 V vs. Ag under various temperature for 3000 s: (a) 303 K, (b) 333 K, (c) 353 K and (d) 373 K. (e) the pore and ligament size distribution of these NPA films.

3. Synthesis of Pd@NPA by GRR approach

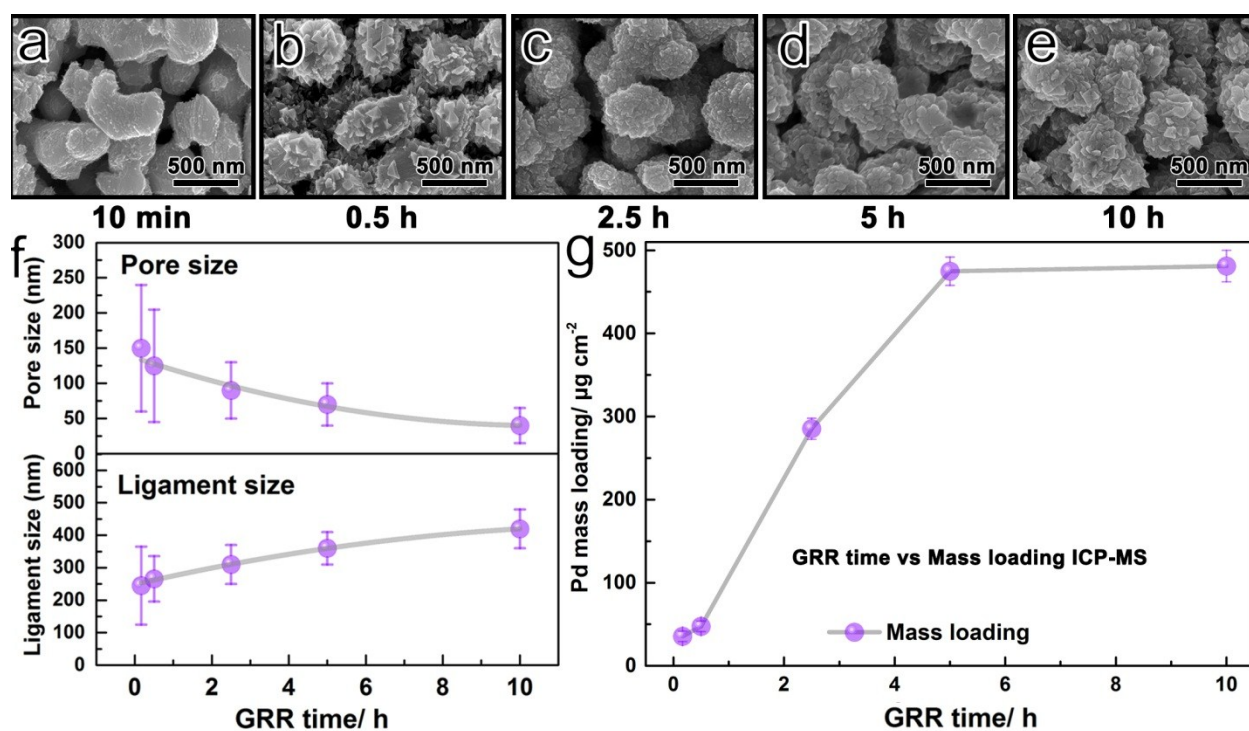


Figure S8. (a-e) SEM images of Pd@NPA samples after GRR with various immersion time (from 10 min to 10 h). (f) The corresponding ligament and pore size distribution of these Pd@NPA samples and (g) their Pd mass loading as a function of GRR time.

The as-prepared 3D NPA provides a flexible substrate for the in-situ growth of Pd coatings by a spontaneous galvanic replacement reaction (GRR). Compared with conventional aqueous solutions, Ethaline provides a novel solvent environment (low water activity with large surface tension and highly ordered hydrogen bonding) to guide

the evolution of nanoarchitected materials. The morphology evolution of the resulting Pd-modified NPA samples fabricated by the replacement reaction at 373 K with various immersion time (from 10 min to 10 h) under a normal atmosphere with an open system was carefully investigated (Figure S8a-e). It can be observed that the obtained Pd@NPA with 10 min GGR time shows 3D interconnected porous configuration with slightly coarsened ligament surface (Figure S8a). When the GGR time is increased to 0.5 h, the ligament of Pd@NPA becomes rougher and packaged with angular nanoparticles on the ligament surface (Figure S8b). After reacting for 2.5 h, the 3D interconnected porous structure is well retained, and the ligaments are obviously coarsened and fully covered with nanoparticles (Figure S8c). When the GGR time reaches 5 h, the 3D porous skeletons of NPA appears partially damaged and some pores are clogged by the coarsened ligaments (Figure S8d). Further extending the GGR time to 10 h, the resulting Pd@NPA maintains similar nanostructure to the one obtained at 5 h, revealing a reaction termination owing to the steric effect induced by the surface coverage of Pd on the NPA, which blocks the reaction channel. In addition, both the pore and ligament size changes along with the GGR time that are derived from SEM images by statistical measurements also reveal the structure evolution of Pd@NPA. The pore size is gradually decreased, while the ligament size is accordingly increased along with increase in the Pd mass loading upon the GRR process. These results reveal that both nanostructure and Pd mass loading can be tuned by changing the GGR time. To achieve efficient utilization of Pd and obtain an expected 3D interconnected porous architecture, a short GRR time of 0.5 h is selected for the subsequent studies.

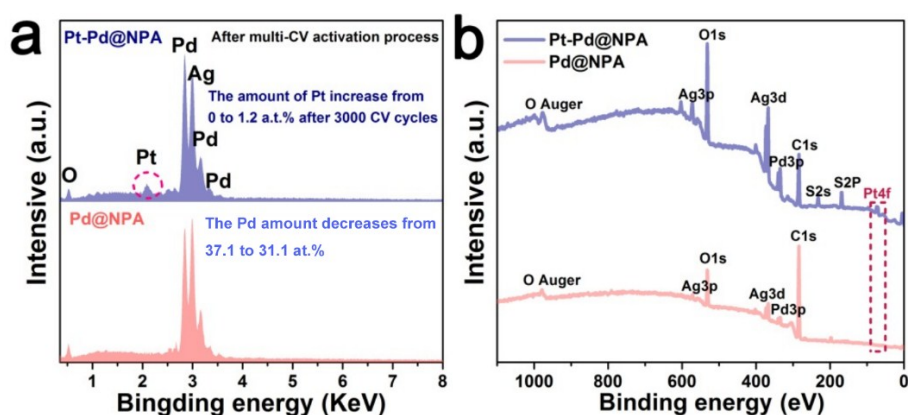


Figure S9. (a) EDS and (b) XPS surveys of the pristine Pd@NPA before and after 3000th CV cycles between +200 and -200mV vs. RHE at 100 mV s^{-1} in $0.5 \text{ M H}_2\text{SO}_4$.

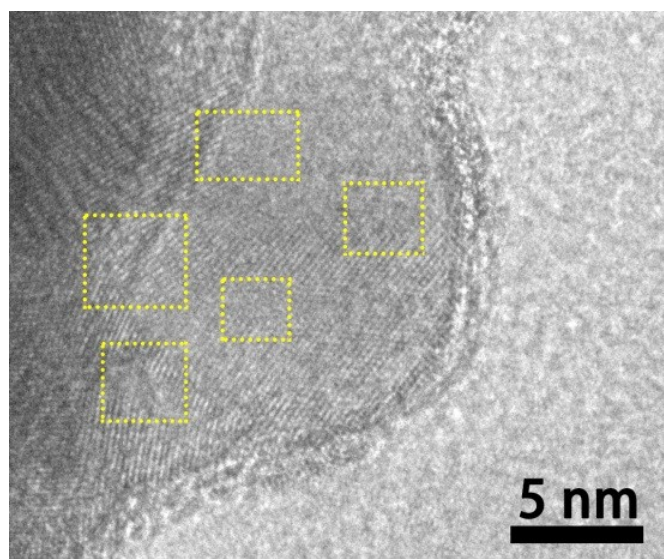


Figure S10. HR-TEM image of Pt-Pd@NPA, the yellow dashed boxes mark some interfacial dislocations in Pt-Pd@NPA.

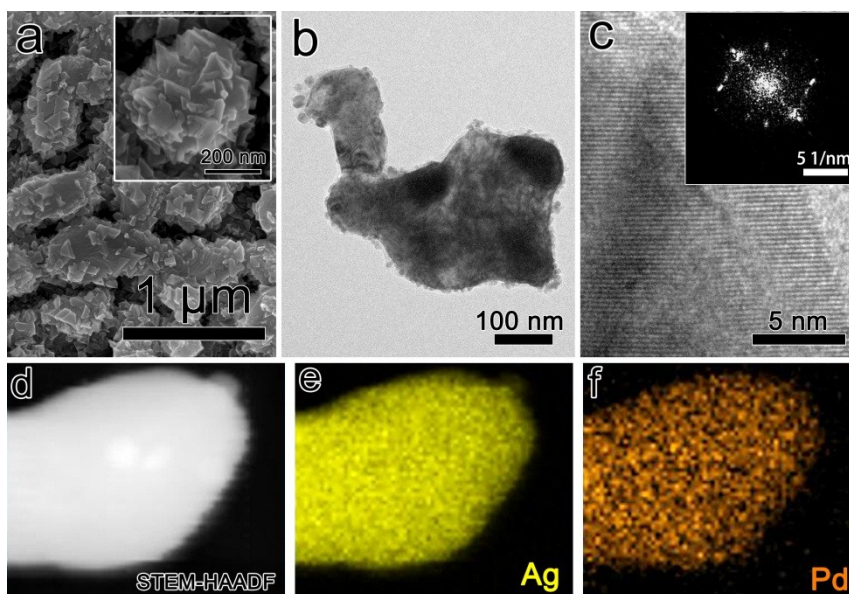


Figure S11. Structure of pristine Pd@NPA. (a) SEM image of Pd@NPA, (b) TEM image of Pd@NPA, (c) HR-TEM image of Pd@NPA (inset shows the FFT pattern). (d) STEM-HAADF image of Pd@NPA, (e) and (f) the EDS elemental mapping of Ag and Pd in the ligament of Pd@NPA sample.

The typical SEM image of the as-prepared Pd@NPA with 0.5 h GRR time is shown in Figure S11a. The corresponding TEM image of a single ligament of Pd@NPA, shown in Figure S11b, confirms its rough surface with nanoparticles grown on the surface. The corresponding HR-TEM image indicates the monocrystalline nature of the Pd@NPA (Figure 11c). Further HAADF-STEM analysis and associated EDS mapping reveal the uniform distribution of Ag and Pd elements throughout the ligament of the Pd@NPA.

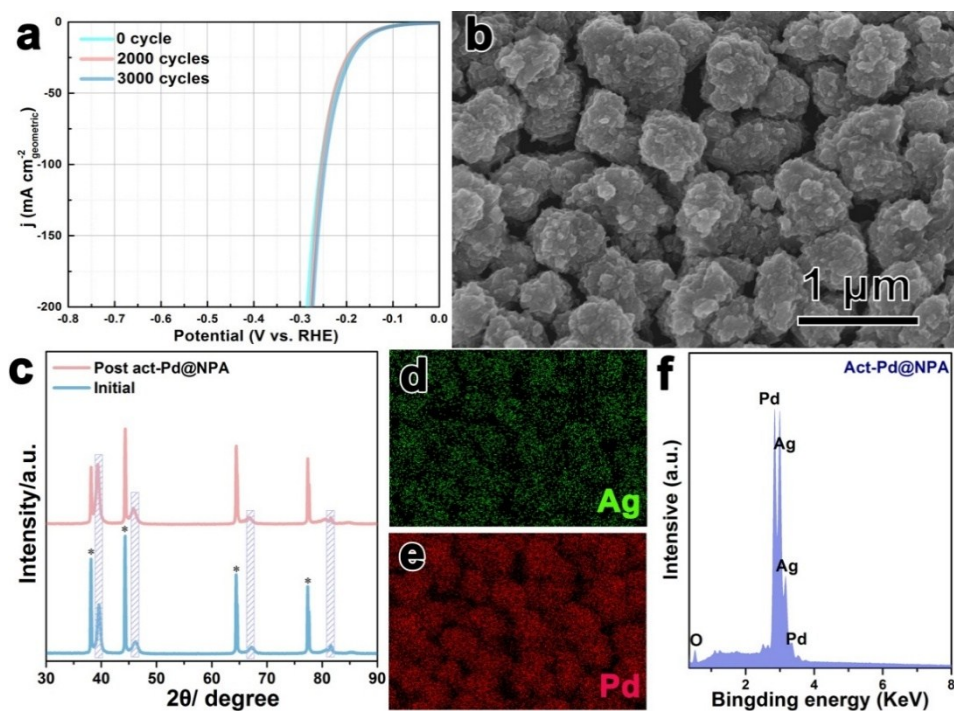


Figure S12. Characterization of the Pd@NPA after multi-CV cycling activation with graphite as the counter electrode. (a) Polarization curves of Pd@NPA electrode before and after continuous CV cycling activation between ± 200 mV vs. RHE at 100 mV s^{-1} in $0.5 \text{ M H}_2\text{SO}_4$. The graphite rod was served as the counter electrode to eliminate the Pt contamination. The HER activity of post-Pd@NPA maintains stable with the increasing CV cycles (0-3000th), (b) SEM image of Pd@NPA after 3000th cycles, which shows no obvious morphology change before and after activation. (c) XRD pattern of the Pd@NPA after 3000th cycles shows no phase change. (d-f) EDS elemental mapping of Pd@NPA after 3000th cycles indicates uniform distribution Pd and Ag on the surface without the contamination of Pt.

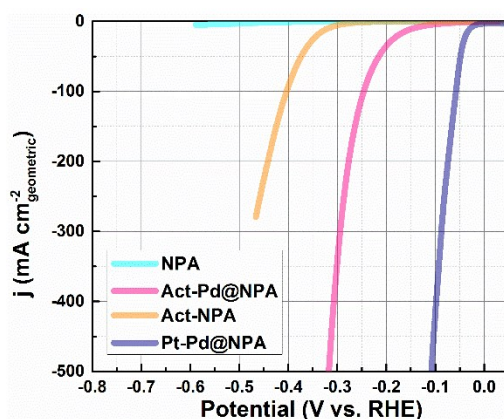


Figure S13. Polarization curves of pristine NPA, Pd@NPA with 0.5 h GRR time, as well as NPA and Pd@NPA after 3000th potential cycling activation process.

As expected, the pristine NPA shows negligible HER activity, while its catalytic activity (act-NPA) is observed to significantly enhance after multi CV activation due to the deposition of Pt on NPA. Even so, the act-NPA still shows far inferior catalytic activity in comparison with both Pd@NPA and act-Pd@NPA. This result indicates that the superior HER activity of act-Pd@NPA (Pt-Pd@NPA) can be mainly ascribed to the synergistic effect between the

4. Potential cycling activation process

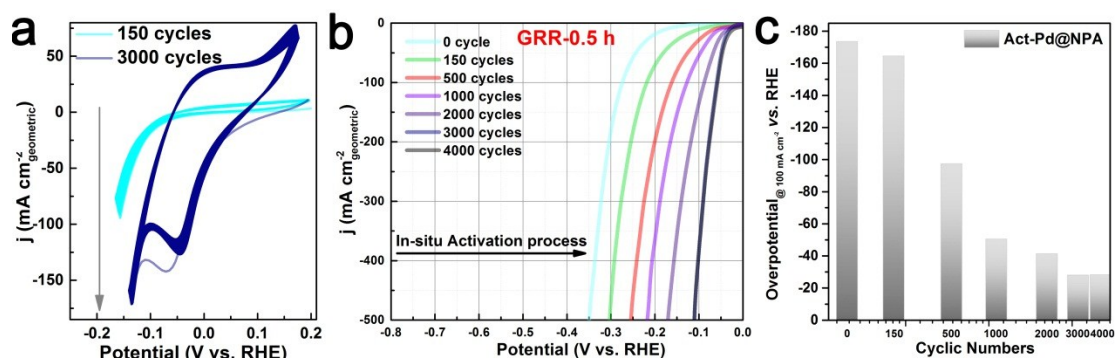


Figure S14. (a) Multi CV cycling curves of Pd@NPA sample for 0.5 h GRR at 373 K (Pd@NPA-0.5) with various cycling numbers at 100 mV s^{-1} in $0.5 \text{ M H}_2\text{SO}_4$. (b) Polarization curves of Pd@NPA-0.5 obtained after different consecutive CV cycles (initial, 150, 500, 1000, 2000, 3000 and 4000 cycles) from +200 to -200 mV vs. RHE at 100 mV s^{-1} in $0.5 \text{ M H}_2\text{SO}_4$ and (c) comparison of overpotentials for 10 mA cm^{-2} at various stages of activation.

Figure S14a shows the potential cycling process of act-Pd@NPA at initial (0-150th) and final (3000th-4000th) stage, it is observed that HER activity of act-Pd@NPA enhances successively during the activation process (Figure S14b), as the response catalytic current shows significant improvements at the same applied overpotentials. In addition, the newborn reduction peak of CV curves upon activation (3000th-4000th) around -0.03 V vs. RHE is associated with underpotential electrodeposition/desorption of H on Pt surface,¹⁶ which is consistent with the corresponding EDS and XPS surveys (Figure S9) on the pristine Pd@NPA before and after 3000th CV cycles, revealing the grafting of Pt on the catalyst surface. The derived LSV data (Figure S14c, overpotentials at 10 mA cm^{-2}) further quantitatively illustrates the promoting HER activity of Pt-Pd@NPA after continuous CV activation process. In particular, the HER activity is found to stabilize after 3000th potential cycling operation, suggesting the optimized activation cycles.

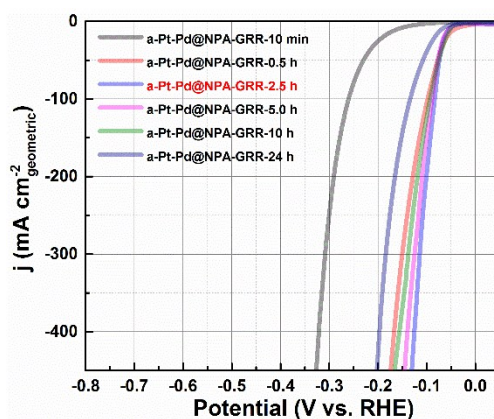


Figure S15. Polarization curves of Pd@NPA samples with different GRR time after 3000th potential cycling activation process. It can be seen that act-Pt-Pd@NPA with 0.5-24 h exhibit approximate HER activity. Taking the Pd mass loading into consideration (Figure S8), the act-Pt-Pd@NPA-0.5 can be served as the optimal candidate catalyst.

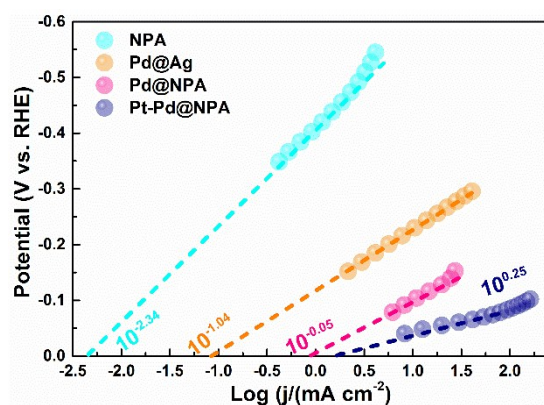


Figure S16. Exchange current density for HER of various as-prepared catalysts (as indicated) in acidic media from the corresponding Tafel plots by extrapolation method.

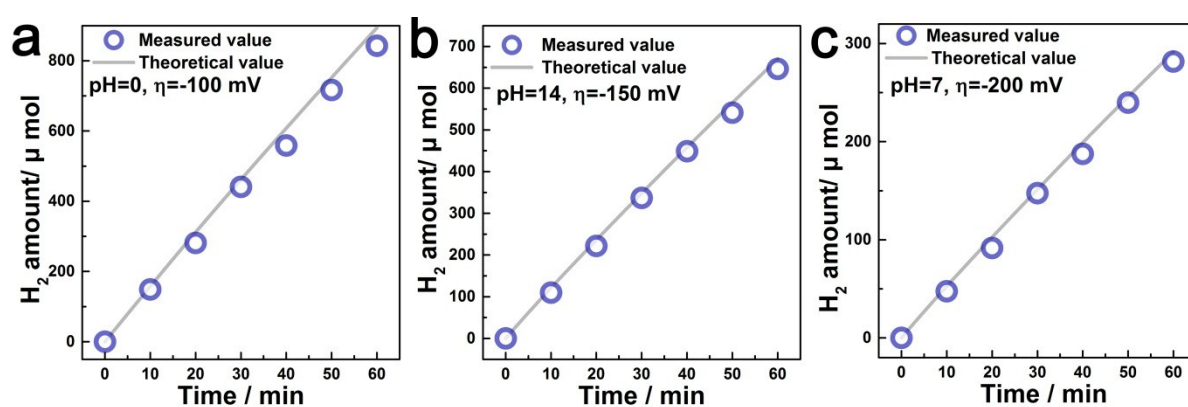


Figure S17 The experimentally amount of H₂ generated by Pt-Pd@NPA (identified by gas chromatography analysis) and theoretically calculated amount vs. time at various pH values, (a) at overpotential of -100 mV for pH=0, (b) at overpotential of -150 mV for pH=14 and (c) at overpotential of -200 mV for pH=7.

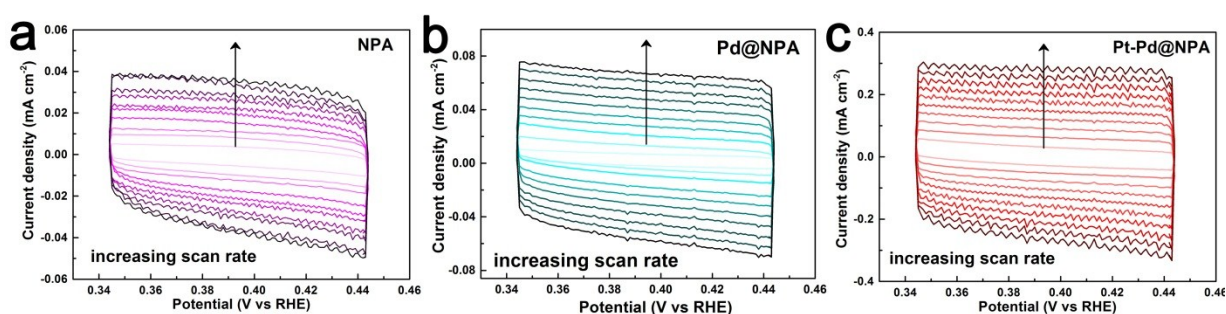


Figure S18. Electrochemical capacitance measurements to determine the electrochemical active surface area (ECSA) of the NPA substrate, Pd@NPA and Pt-Pd@NPA. The capacitive current from double layer charging can be measured from CVs in a potential where no faradaic process are observed. CV of (a) NPA, (b) Pd@NPA and (c) Pt-Pd@NPA in the 0.5 M H₂SO₄ electrolyte, at various scan rates from 20 to 200 mV s⁻¹.

5. Stability of Pt-Pd@NPA

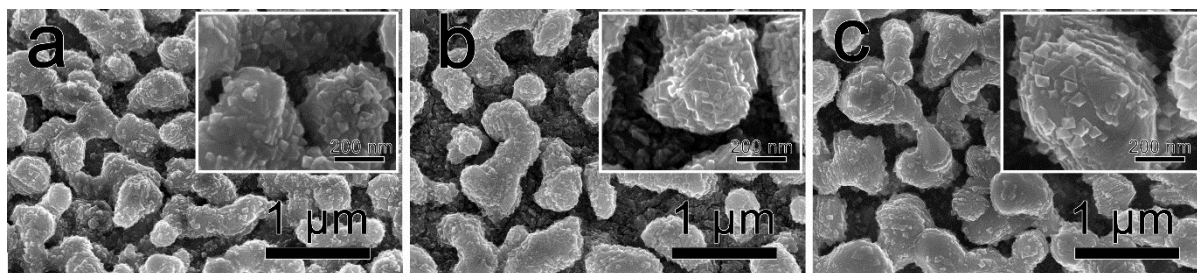


Figure S19. SEM images of Pt-Pd@NPA after 100 h long-term HER electrocatalysis at 1000 mA cm^{-2} in 1.0 M KOH (a), 1.0 M PBS (b) and 0.5 M H_2SO_4 (c) insets show the corresponding high magnification image. These results indicate that the morphology remains the initial 3D configuration without dissolving or peeling off from the substrate.

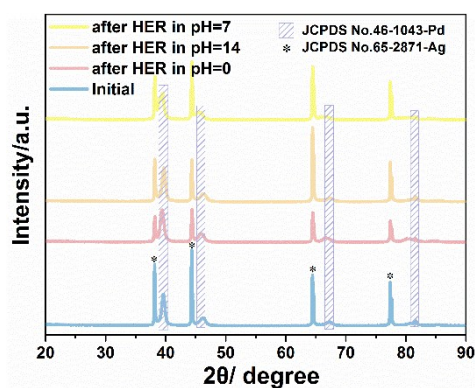


Figure S20. XRD pattern of Pt-Pd@NPA after 100 h long-term HER electrocatalysis at 1000 mA cm^{-2} in 1.0 M KOH (a), 1.0 M PBS (b) and 0.5 M H_2SO_4 . The major characteristic peaks of these four samples (mark asterisk) are attributed to the Ag substrate (JCPDS No: 65-2871), while other peaks can be assigned to metallic Pd phase (JCPDS No: 46-1043).

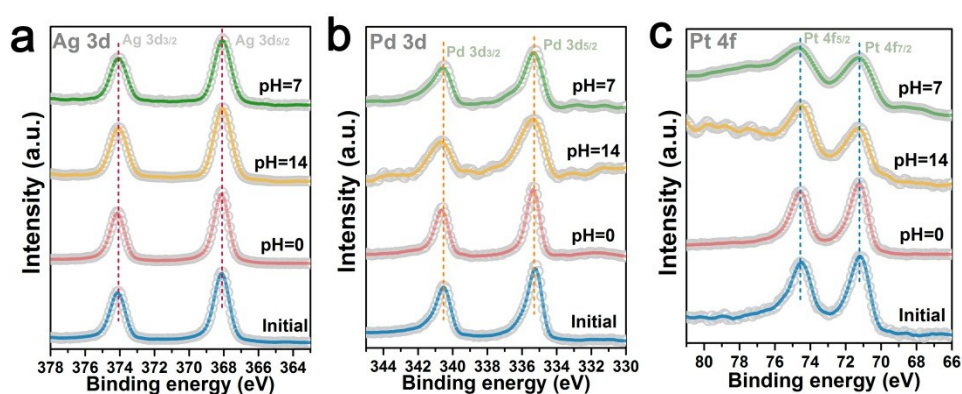


Figure S21. High-resolution XPS patterns of Ag 3d (a), Pd 3d (b) and Pt 4f (c) of the Pt-Pd@NPA catalyst before and after long-term HER over a wide pH range at 1000 mA cm^{-2} for 100 h.

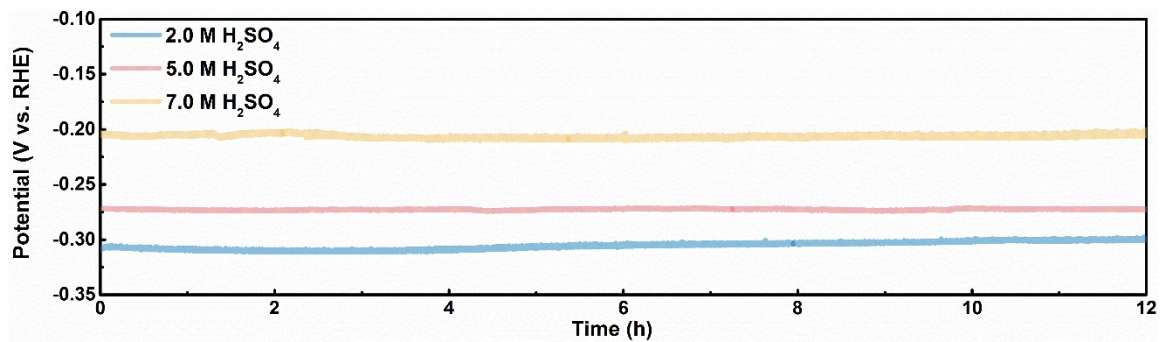


Figure S22. Chronopotential curves of Pt-Pd@NPA obtained in extremely acidic condition (from 2-7 M H₂SO₄) at 1000 mA cm⁻² for 12 h.

Table S1. Comparison of the electrochemical activities of as-prepared Pt-Pd@NPA catalysts for HER with some representative solid-state precious metal-based catalysts reported under acidic electrolyte (0.5 M H₂SO₄).

| Catalyst | η_{onset} (mV) | η_{10} (mV) | η_{100} (mV) | Tafel slope (mV dec ⁻¹) | j_0 (mA cm ⁻²) | Mass loading ($\mu\text{g cm}^{-2}$) | Reference |
|-------------------------------|-------------------------------|---------------------|----------------------|--|---------------------------------|--|------------------|
| Pt-Pd@NPA | 11.7 | 28.1 | 57.7 | 31.2 | 1.78 | 32.53 Pd + 4.96 Pt | This work |
| Pt-VGNsAs | 10 | 60 | - | 28.5 | - | 41.92 Pt | 17 |
| Pd@PdPt | 15 | 39 | ca.90 | 38 | 0.91 | - | 18 |
| Pt@DNA-GC | - | 210 | >290 | 24.1 | - | 15-pt | 19 |
| Pt-Pd/PSiF | - | 45 | - | 42 | - | - | 20 |
| Pt-Pd/PSiF-eRGO | - | 245 | - | 40 | - | - | 20 |
| Pt-Rh/PSiF | - | 83 | - | 51 | - | - | 20 |
| Pt-Ru/PSiF | - | 61 | - | 47 | - | - | 20 |
| Pt-TaS ₂ | | ca.35 | - | 54 | - | - | 21 |
| MoS ₂ -NPAu | 118 | 266 | - | 46 | 0.000419 | - | 22 |
| Pt ML/Au NF/Ni | 40 | 100 | >400 | 53 | - | 0.55-Pt | 3 |
| 3.5 nm Pt/Ni foam | 40 | 110 | >260 | - | - | - | 23 |
| Pd octahedron | 120 | 220 | 340 | 98 | 0.064 | 140-Pd | 24 |
| Pd@L-PtCu | - | ca.50 | ca.150 | 23.5 | - | 110.1-Pt | 25 |
| Pt particles-SnS ₂ | 32 | 117 | >310 | 69 | 0.39 | 118-Pt | 26 |
| Pt-MoS ₂ | 31 | 86 | >300 | 52 | 0.256 | 66-Pt | 27 |

References

1. Ng, J. W. D.; García-Melchor, M.; Bajdich, M.; Chakthranont, P.; Kirk, C.; Vojvodic, A.; Jaramillo, T. F., Gold-supported cerium-doped NiOx catalysts for water oxidation. *Nature Energy* 2016, 1, 16053.
2. Kibsgaard, J.; Jaramillo, T. F., Molybdenum phosphosulfide: an active, acid-stable, earth-abundant catalyst for the hydrogen evolution reaction. *Angewandte Chemie* 2014, 53, 14433-7.
3. Li, M.; Ma, Q.; Zi, W.; Liu, X.; Zhu, X.; Liu, S. F., Pt monolayer coating on complex network substrate with high catalytic activity for the hydrogen evolution reaction. *Science advances* 2015, 1, e1400268-e1400268.
4. Benck, J. D.; Chen, Z.; Kuritzky, L. Y.; Forman, A. J.; Jaramillo, T. F., Amorphous Molybdenum Sulfide Catalysts for Electrochemical Hydrogen Production: Insights into the Origin of their Catalytic Activity. *ACS Catalysis* 2012, 2, 1916-1923.
5. Yang, C.; Gao, M. Y.; Zhang, Q. B.; Zeng, J. R.; Li, X. T.; Abbott, A. P., In-situ activation of self-supported 3D hierarchically porous Ni₃S₂ films grown on nanoporous copper as excellent pH-universal electrocatalysts for hydrogen evolution reaction. *Nano Energy* 2017, 36, 85-94.
6. Gu, Y.; Chen, S.; Ren, J.; Jia, Y. A.; Chen, C.; Komarneni, S.; Yang, D.; Yao, X., Electronic Structure Tuning in Ni₃FeN/r-GO Aerogel toward Bifunctional Electrocatalyst for Overall Water Splitting. *ACS nano* 2018, 12, 245-253.
7. Wu, M.-S.; Wang, M.-J.; Jow, J.-J., Fabrication of porous nickel oxide film with open macropores by electrophoresis and electrodeposition for electrochemical capacitors. *Journal of Power Sources* 2010, 195, 3950-3955.
8. Zhang, J.; Li, C. M., Nanoporous metals: fabrication strategies and advanced electrochemical applications in catalysis, sensing and energy systems. *Chemical Society reviews* 2012, 41, 7016-31.
9. Tuan, N. T.; Park, J.; Lee, J.; Gwak, J.; Lee, D., Synthesis of nanoporous Cu films by dealloying of electrochemically deposited Cu-Zn alloy films. *Corrosion Science* 2014, 80, 7-11.
10. Xiao, B.; Yuan, Q., Nanoporous metal organic framework materials for hydrogen storage. *Particuology* 2009, 7, 129-140.
11. Cherevko, S.; Xing, X.; Chung, C.-H., Electrodeposition of three-dimensional porous silver foams. *Electrochemistry Communications* 2010, 12, 467-470.
12. Zhang, Q. B.; Abbott, A. P.; Yang, C., Electrochemical fabrication of nanoporous copper films in choline chloride-urea deep eutectic solvent. *Physical chemistry chemical physics : PCCP* 2015, 17, 14702-9.
13. Yang, C.; Zhang, Q. B.; Gao, M. Y.; Hua, Y. X.; Xu, C. Y., In Situ Electrochemical Fabrication of Three Dimensional Hierarchical Nanoporous Copper Films and Their Electrocatalytic Performance. *Journal of The Electrochemical Society* 2016, 163, D469-D475.
14. Qiu, H. J.; Peng, L.; Li, X.; Xu, H. T.; Wang, Y., Using corrosion to fabricate various nanoporous metal structures. *Corrosion Science* 2015, 92, 16-31.
15. Lin, Y.-W.; Tai, C.-C.; Sun, I. W., Electrochemical Preparation of Porous Copper Surfaces in Zinc Chloride-1-ethyl-3-methyl Imidazolium Chloride Ionic Liquid. *Journal of The Electrochemical Society* 2007, 154, D316.
16. Chen, R.; Yang, C.; Cai, W.; Wang, H.-Y.; Miao, J.; Zhang, L.; Chen, S.; Liu, B., Use of Platinum as the Counter Electrode to Study the Activity of Nonprecious Metal Catalysts for the Hydrogen Evolution Reaction. *ACS Energy Letters* 2017, 2, 1070-1075.
17. Zhang, H.; Ren, W.; Guan, C.; Cheng, C., Pt decorated 3D vertical graphene nanosheet arrays for efficient methanol oxidation and hydrogen evolution reactions. *J. Mater. Chem. A* 2017, 5, 22004-22011.
18. Liu, Y.; Liu, S.; Che, Z.; Zhao, S.; Sheng, X.; Han, M.; Bao, J., Concave octahedral Pd@PdPt electrocatalysts integrating core-shell, alloy and concave structures for high-efficiency oxygen reduction and hydrogen evolution reactions. *Journal of Materials Chemistry A* 2016, 4, 16690-16697.

19. Anantharaj, S.; Karthik, P. E.; Subramanian, B.; Kundu, S., Pt Nanoparticle Anchored Molecular Self-Assemblies of DNA: An Extremely Stable and Efficient HER Electrocatalyst with Ultralow Pt Content. *ACS Catalysis* 2016, 6, 4660-4672.
20. Ensafi, A. A.; Jafari-Asl, M.; Rezaei, B., Graphene/nano-porous silicon and graphene/bimetallic silicon nanostructures (Pt-M, M: Pd, Ru, Rh), efficient electrocatalysts for the hydrogen evolution reaction. *Physical chemistry chemical physics : PCCP* 2015, 17, 23770-82.
21. Zeng, Z.; Tan, C.; Huang, X.; Bao, S.; Zhang, H., Growth of noble metal nanoparticles on single-layer TiS₂ and TaS₂ nanosheets for hydrogen evolution reaction. *Energy Environ. Sci.* 2014, 7, 797-803.
22. Tan, Y.; Liu, P.; Chen, L.; Cong, W.; Ito, Y.; Han, J.; Guo, X.; Tang, Z.; Fujita, T.; Hirata, A.; Chen, M. W., Monolayer MoS₂ films supported by 3D nanoporous metals for high-efficiency electrocatalytic hydrogen production. *Advanced materials* 2014, 26, 8023-8.
23. Luo, J.; Im, J.-H.; Mayer, M. T.; Schreier, M.; Nazeeruddin, M. K.; Park, N.-G.; Tilley, S. D.; Fan, H. J.; Grätzel, M., Water photolysis at 12.3% efficiency via perovskite photovoltaics and Earth-abundant catalysts. *Science* 2014, 345, 1593-1596.
24. Li, J.; Zhou, P.; Li, F.; Ma, J.; Liu, Y.; Zhang, X.; Huo, H.; Jin, J.; Ma, J., Shape-controlled synthesis of Pd polyhedron supported on polyethyleneimine-reduced graphene oxide for enhancing the efficiency of hydrogen evolution reaction. *Journal of Power Sources* 2016, 302, 343-351.
25. Ren, F.; Lu, H.; Liu, H.; Wang, Z.; Wu, Y.; Li, Y., Surface ligand-mediated isolated growth of Pt on Pd nanocubes for enhanced hydrogen evolution activity. *Journal of Materials Chemistry A* 2015, 3, 23660-23663.
26. Liu, G.; Qiu, Y.; Wang, Z.; Zhang, J.; Chen, X.; Dai, M.; Jia, D.; Zhou, Y.; Li, Z.; Hu, P., Efficiently Synergistic Hydrogen Evolution Realized by Trace Amount of Pt-Decorated Defect-Rich SnS₂ Nanosheets. *ACS applied materials & interfaces* 2017, 9, 37750-37759.
27. Ren, W.; Zhang, H.; Cheng, C., Ultrafine Pt nanoparticles decorated MoS₂ nanosheets with significantly improved hydrogen evolution activity. *Electrochimica Acta* 2017, 241, 316-322.